Thermal Science and Engineering 2026, 9(1), 6665.
https://doi.org/10.24294/tse6665

Article

Numerical design and simulation of an n-i-p type heterostructure lead-free perovskite solar cell using SCAPS

Anchal Srivastava, Anjali Gupta, Rajesh Kumar Shukla*, and Nidhi Singh

Department of Physics, University of Lucknow, Lucknow-226007, India
* **Corresponding author:** Rajesh Kumar Shukla, rajeshkumarshukla00@gmail.com

CITATION

Srivastava A, Gupta A, Shukla RK, Singh N. Numerical design and simulation of an n-i-p type heterostructure lead-free perovskite solar cell using SCAPS. Thermal Science and Engineering. 2026; 9(1): 6665.
https://doi.org/10.24294/tse6665

ARTICLE INFO

Received: 27 May 2024
Accepted: 10 June 2026
Available online: 06 July 2026

Highlights

- Full device modelling of the $CH_3NH_3SnCl_3$/$CH_3NH_3SnBr_3$/$CH_3NH_3SnI_3$ tin-halide n-i-p perovskite heterostructure was performed with SCAPS-1D.
- $CH_3NH_3SnCl_3$ functions as the optimised ETL and $CH_3NH_3SnI_3$ as the optimised HTL; $CH_3NH_3SnBr_3$ is the intrinsic absorber.
- The absorber optimum trap density is $N_t = 10^{10}$ cm^{-3} and the optimum thickness is 750 nm.
- A complete set of optimised design parameters for halogen-based perovskite solar cell structures was established.
- The optimised $CH_3NH_3SnBr_3$-absorber perovskite solar cell achieved a power conversion efficiency of 31.11%.

Abstract: Tin-based halide perovskites have drawn considerable scientific attention as promising candidates for next-generation photovoltaic devices, primarily because they circumvent the toxicological and regulatory challenges associated with lead-containing counterparts. In the present work, a lead-free n-i-p type perovskite heterostructure solar cell was numerically designed and systematically optimized via the one-dimensional Solar Cell Capacitance Simulator (SCAPS-1D). The proposed device adopts the configuration FTO/$CH_3NH_3SnCl_3$/$CH_3NH_3SnBr_3$/$CH_3NH_3SnI_3$/Au, in which the tin chloride perovskite functions as the electron transport layer (ETL), the tin bromide perovskite serves as the intrinsic absorber, and the tin iodide perovskite acts as the hole transport layer (HTL). A systematic parametric investigation was carried out, covering layer thickness, electron affinity, shallow doping concentration, and trap-state density for each functional layer. Simulation outcomes demonstrate that an absorber thickness of 750 nm yields the best balance between photon harvesting and charge-carrier collection. Furthermore, elevated doping in the absorber was found to reduce device performance through enhanced Shockley–Read–Hall (SRH) recombination, while a reduced trap density markedly improved all photovoltaic figures of merit. Following comprehensive optimization, the device achieved a power conversion efficiency (PCE) of 31.11%, a short-circuit current density (J_{SC}) of 33.89 mA/cm², an open-circuit voltage (V_{OC}) of 1.0410 V, and a fill factor (FF) of 88.18%. The influence of ambient temperature was also studied, revealing that 300 K represents the optimal operating condition. The findings underline the viability of all-tin halide perovskite architectures for sustainable, high-efficiency photovoltaics.

Keywords: SCAPS-1D simulation; lead-free perovskite; tin halide; photovoltaics; $CH_3NH_3SnX_3$; power conversion efficiency

1. Introduction

The accelerating global transition toward clean energy has positioned photovoltaic (PV) technology at the forefront of renewable power generation research. Among all known light-harvesting materials, sunlight offers an unparalleled combination of abundance, universality, and environmental neutrality compared with depletable fossil-fuel resources [1,2]. Within the broad landscape of PV materials, organic-inorganic metal halide perovskites have risen to prominence over the preceding decade, with laboratory-scale devices now routinely surpassing PCEs of 25% [3–5]. Nonetheless, the inherent toxicity of lead, the metallic cation at the heart of the best-performing perovskite compositions, represents a critical barrier to large-scale commercialization, since current and forthcoming environmental legislation strictly limits or prohibits lead in consumer electronic products [6].

To circumvent the lead problem, intensive research efforts have been directed at replacing Pb^{2+} with lower-toxicity divalent or multivalent cations. Tin (Sn^{2+}), bismuth (Bi^{3+}), antimony (Sb^{3+}), copper (Cu^{2+}), and germanium (Ge^{2+}) are among the principal candidates that have been explored in the $APbX_3$ perovskite lattice [7–9]. Of these, tin-based perovskites have attracted the greatest attention because Sn^{2+} is iso-electronic with Pb^{2+} and produces materials with comparably suitable band gaps. Reported PCEs for tin perovskite devices have reached up to 13%, and their intrinsically narrower optical band gaps together with higher charge-carrier mobilities represent genuine advantages relative to lead analogues [10–14]. A persistent limitation, however, is the susceptibility of Sn^{2+} to oxidation to Sn^{4+} upon air exposure, which introduces deep trap states that degrade charge transport [2,15,16]. Parallel simulation and experimental studies conducted in our laboratory have further corroborated these trends [17–23].

Despite these encouraging efficiencies, the thermodynamic limit for single-junction devices, the Shockley-Queisser ceiling of approximately 33.7%, remains well out of reach for most lead-free formulations [24–27]. Strategies to push beyond this boundary using nanoscale plasmonic or photonic structures have been demonstrated for lead-based cells [28–31], but analogous demonstrations in lead-free systems remain scarce. Multiple oxidation-mitigation pathways are under active exploration, including structural encapsulation, electronic passivation through interface engineering, hydrophobic surface coatings, and hydrogen-bond-mediated crystallographic stabilisation [32–36].

Closing the efficiency gap between lead-free and lead-based cells is a key objective for the field [37]. Computational device modelling provides an efficient, low-cost route to screen materials and device architectures prior to fabrication. Numerical platforms such as SCAPS, ASA, AMPS-1D, ADEPT, ASPIN, Sentaurus, PECSIM, SETFOS, SILVACO ATLAS, TCAD, wxAMPS-1D, AFORS-HET, and GPVDM have each been applied to this end, enabling systematic identification of efficiency-limiting factors and optimal device configurations [38,39-42].

The present work employs SCAPS-1D (version 3.3.10), a widely adopted one-dimensional semiconductor device simulator developed by Professor Marc Burgelman and colleagues at the Department of Electronics and Information Systems (ELIS), University of Ghent, Belgium [37-43]. Originally conceived for

polycrystalline thin-film architectures such as a-Si, CdTe, and CIGS, the simulator has since been extended to cover silicon and perovskite cells. Its computational framework accommodates up to seven active layers, each with three independent deep-level defect states. Key output parameters include V_{OC}, J_{SC}, FF, PCE, quantum efficiency (QE%), generation and recombination profiles, and energy band diagrams, all of which can be extracted under illuminated conditions across a range of temperatures and irradiances.

Carrier recombination in the bulk is treated within the Shockley-Read-Hall (SRH) formalism, while interfacial recombination is handled by a generalised extension of the same approach. The physical backbone of SCAPS-1D consists of three coupled differential equations-Poisson's equation, the electron continuity equation, and the hole continuity equation-solved self-consistently in one spatial dimension, as detailed in the literature [40,44,45].

Poisson equation:

$$dE/dx = -d^2\Psi/dx^2 = (q/\varepsilon)[p(x) - n(x) + N_D^+(x) - N_A^-(x) + p_t(x) - n_t(x)] \quad (1)$$

In the above expression, E denotes the electric field, Ψ is the electrostatic potential, q is the elementary charge, ε is the semiconductor permittivity, p and n are the free hole and electron concentrations, N_D^+ and N_A^- are the ionised donor and acceptor densities, and n_t and p_t represent trap-occupied electron and hole densities, respectively. The spatial coordinate is x.

Continuity equations for holes and electrons:

$$dp_n/dt = G_p - (p_n - p_{n0})/\tau_p + p_n\,\mu_p\,(dE/dx) + \mu_p\,E\,(dp_n/dx) + D_p\,(d^2p_n/dx^2) \quad (2)$$

$$dn_p/dt = G_n - (n_p - n_{p0})/\tau_n + n_p\,\mu_n\,(dE/dx) + \mu_n\,E\,(dn_p/dx) + D_n\,(d^2n_p/dx^2) \quad (3)$$

Here, G_n and G_p represent the electron and hole generation rates, while D_n and D_p denote their respective diffusion coefficients.

Drift–diffusion transport equations:

$$J_n(x) = qn\mu_n E + qD_n\,(dn/dx) = n\mu_n\,(dE_{Fn}/dx) \quad (4)$$

$$J_p(x) = qp\mu_p E + qD_p\,(dp/dx) = p\mu_p\,(dE_{Fp}/dx) \quad (5)$$

where μ_n and μ_p are the electron and hole mobilities, and E_{Fn} and E_{Fp} are the quasi-Fermi energies for electrons and holes, respectively.

The primary objective of this study is to enhance the photovoltaic performance of a $CH_3NH_3SnCl_3$-based solar cell through systematic parameter optimisation within the SCAPS-1D framework. Metal oxide electron transport layers, and specifically ZnO, were considered for their favourable electronic properties, optical transparency, and conformal substrate coverage characteristics that make them well suited to cost-effective, large-area lead-free perovskite device fabrication [44,46].

The optimisation workflow proceeds in sequential stages. First, the ETL is characterised with respect to thickness, electron affinity, shallow donor concentration, and trap density. Subsequently, the same parameter set is evaluated for the absorber and HTL. The influence of the back-contact work function on photovoltaic output is also assessed. The fully optimised device attains a PCE of

approximately 31.11%, a roughly fourfold enhancement over the baseline configuration.

2. Materials and methods

All simulations were performed under AM1.5 G standard illumination (100 mW/cm²) at a fixed operating temperature of 300 K. The absorber layer was sandwiched between the ETL and HTL to replicate the conventional n-i-p device geometry. **Figure 1** presents a schematic cross-section of the proposed device architecture, comprising fluorine-doped tin oxide (FTO) as the transparent front contact, $CH_3NH_3SnCl_3$ as the n-type ETL, $CH_3NH_3SnBr_3$ as the intrinsic absorber, $CH_3NH_3SnI_3$ as the p-type HTL, and gold (Au) as the back contact. In the n-i-p configuration, photons enter through the FTO/ETL side and are absorbed primarily within the $CH_3NH_3SnBr_3$ interlayer.

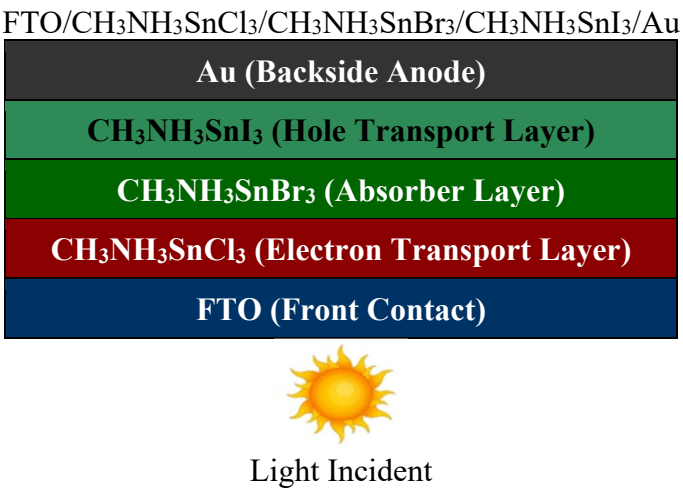

Figure 1. Cross-sectional schematic of the $FTO/CH_3NH_3SnCl_3/CH_3NH_3SnBr_3/CH_3NH_3SnI_3/Au$, n-i-p perovskite solar cell architecture under investigation.

The initial material parameters used to seed the simulation were sourced from theoretical calculations, experimentally measured values, and peer-reviewed literature, and are compiled in **Table 1**. The subsequent optimization steps systematically varied the ETL thickness, electron affinity, shallow donor doping (N_D), and trap density (N_t), followed by equivalent investigations for the absorber and HTL. The back-contact work function was also varied to assess its impact. Interfacial defect parameters for the n/i and i/p junctions are listed in **Table 2**.

Table 1. Initial physical parameters of $CH_3NH_3SnI_3$, $CH_3NH_3SnBr_3$, $CH_3NH_3SnCl_3$, and FTO used in the FTO/$CH_3NH_3SnCl_3$/$CH_3NH_3SnBr_3$/$CH_3NH_3SnI_3$/Au PSC.

Physical Parameters	**Symbol**	**Unit**	**$CH_3NH_3SnI_3$ (HTL)**	**$CH_3NH_3SnBr_3$ (Absorber Layer)**	**$CH_3NH_3SnCl_3$ (ETL)**	**FTO**
Thickness	t	nm	300	100	300	300
Energy Band Gap	E_g	eV	1.3	1.3	3.2	3.5
Electron Affinity	χ	eV	3.9	4.17	3.71	4.0
Relative Dielectric Permittivity	ε_r	–	6.5	10.0	6.5	9.0
Effective Valence Band DOS	N_V	cm^{-3}	1×10^{18}	2.2×10^{18}	1×10^{18}	2.2×10^{18}
Effective Conduction Band DOS	N_C	cm^{-3}	1×10^{19}	1.8×10^{18}	1×10^{19}	1.8×10^{19}
Hole Thermal Velocity	V_e	cm/s	1×10^{7}	1×10^{7}	1×10^{7}	1×10^{7}
Electron Thermal Velocity	V_h	cm/s	1×10^{7}	1×10^{7}	1×10^{7}	1×10^{7}
Electron Mobility	μ_e	$cm^2/V{\cdot}s$	1.6	1.6	1.6	20
Hole Mobility	μ_h	$cm^2/V{\cdot}s$	1.6	1.6	1.6	10
Uniform Shallow Donor Doping	N_D	cm^{-3}	0	1×10^{13}	3.2×10^{18}	2×10^{13}
Uniform Shallow Acceptor Doping	N_A	cm^{-3}	3.2×10^{18}	1×10^{13}	0	0
Defect Density	N_t	cm^{-3}	1×10^{15}	1×10^{15}	1×10^{15}	1×10^{15}
References			40	41	42	47

Table 2. Interfacial defect parameters for the n-$CH_3NH_3SnCl_3$, i-$CH_3NH_3SnBr_3$/n-$CH_3NH_3SnCl_3$, and p-$CH_3NH_3SnI_3$/i-$CH_3NH_3SnBr_3$ junctions.

Parameter	**n-$CH_3NH_3SnCl_3$**	**i-$CH_3NH_3SnBr_3$ / n-$CH_3NH_3SnCl_3$**	**p-$CH_3NH_3SnI_3$ / i-$CH_3NH_3SnBr_3$**
Defect type	Neutral	Neutral	Neutral
Electron capture cross section (cm^2)	1×10^{-14}	1×10^{-14}	1×10^{-14}
Hole capture cross section (cm^2)	1×10^{-14}	1×10^{-14}	1×10^{-14}
Energetic distribution	Gaussian	Single	Single
Energy w.r.t. Reference (eV)	0.65	0.60	0.60
Characteristic energy (eV)	0.1	0.1	0.1
Total density (N_t) (cm^{-2})	4.5×10^{17}	4.5×10^{17}	4.5×10^{17}

3. Results and discussion

This section presents a systematic analysis of how each physical parameter of the ETL, absorber and HTL governs the photovoltaic performance of the proposed device. Parameters were refined sequentially and each optimised value was retained as a fixed input for subsequent stages.

3.1. Influence of ETL ($CH_3NH_3SnCl_3$) thickness

The n-type ETL and p-type HTL are multifunctional layers that facilitate selective charge extraction and simultaneously contribute to optical absorption within the device stack. As a result, their physical thicknesses directly govern the generation rate, transport path length and collection efficiency of photogenerated charge carriers. To determine the optimum ETL thickness, the $CH_3NH_3SnCl_3$ n-layer was swept over the range 10–500 nm while the absorber and HTL thicknesses were held constant at 100 nm and 300 nm, respectively. **Figure 2** illustrates how V_{OC}, J_{SC}, FF, and PCE evolve as a function of ETL thickness. The first three parameters exhibit only modest variation across the entire range. The PCE, however, rises to a well-defined peak of 7.67% at 50 nm and then decreases monotonically at greater thicknesses. This fall-off reflects the lengthening electron transit distance to the front electrode at larger ETL dimensions, which raises the probability of trap-assisted recombination with photogenerated holes. Based on these results, an ETL thickness of 50 nm was adopted for all subsequent calculations.

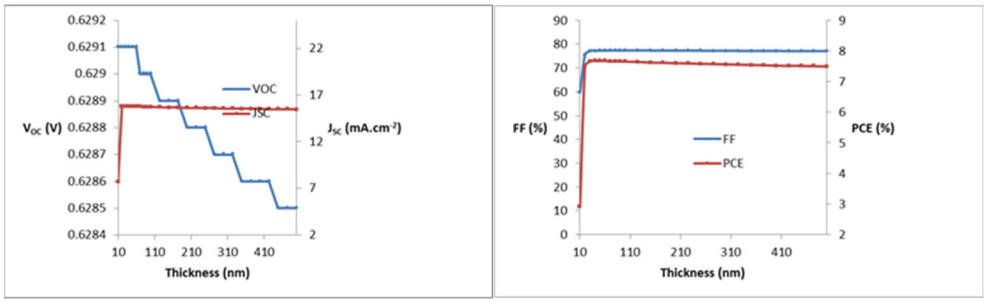

Figure 2. Evolution of V_{OC}, J_{SC}, FF and PCE as a function of ETL ($CH_3NH_3SnCl_3$) thickness.

3.2. Influence of ETL electron affinity

In the second stage of the optimisation, the electron affinity (χ) of the ETL was varied while all other parameters retained the values established in the preceding step. Electron affinity governs the position of the lowest unoccupied molecular orbital (LUMO) in organic frameworks, equivalently, the conduction band minimum in conventional semiconductors, relative to the vacuum level. The appropriate selection of χ determines the degree of energy offset between the ETL and the perovskite absorber, which in turn controls the selectivity of electron injection and the blocking efficiency for holes at the ETL/absorber interface.

As the affinity value (χ) was increased from 3.71 to 4.35 eV, V_{OC} initially declined before stabilising near 4.10 eV, then subsequently rose. J_{SC} decreased monotonically, whereas FF first improved up to χ = 3.77 eV and then fell, yielding a PCE maximum of approximately 7.80% at that affinity value. The corresponding

device parameters at the optimum were V_{OC} = 0.6289 V, J_{SC} = 15.77 mA/cm², and FF = 78.61%. Accordingly, χ = 3.77 eV was selected as the fixed ETL electron affinity for all further simulations, as illustrated in **Figure 3**.

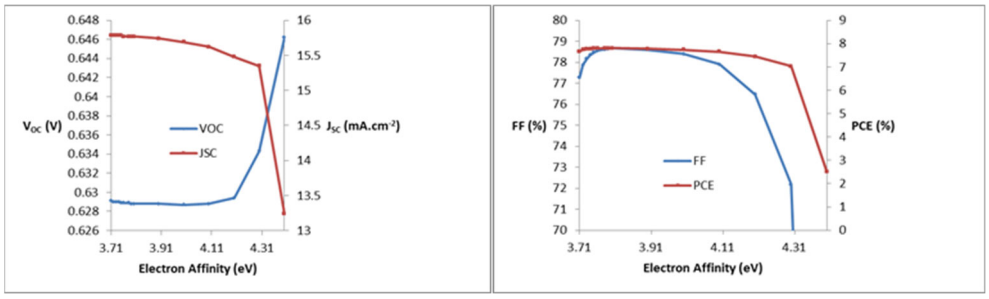

Figure 3. Dependence of V_{OC}, J_{SC}, FF, and PCE on the electron affinity of the ETL ($CH_3NH_3SnCl_3$).

3.3. Influence of ETL donor doping concentration (N_D)

Building upon the optimised ETL thickness (50 nm) and electron affinity (3.77 eV), the donor concentration N_D of the $CH_3NH_3SnCl_3$ ETL was varied from 1 × 10^{18} cm^{-3} to 1 × 10^{22} cm^{-3}. Doping is an essential process for tailoring the charge-transport characteristics of semiconductor layers; it can be implemented through n-type or p-type impurity introduction, or through self-doping mechanisms inherent to certain perovskite compositions. As shown in **Figure 4**, progressive increases in N_D consistently elevated both J_{SC} and FF, leading to a corresponding improvement in PCE. This behaviour is attributable to enhanced energy-level alignment between the ETL conduction band and the perovskite absorber, which suppresses injection barriers and reduces recombination at the ETL/absorber interface. V_{OC} remained essentially constant at ~ 0.6293 V throughout, confirming that the doping level has a negligible influence on the quasi-Fermi level splitting under the conditions studied. A peak PCE of 8.05% was reached at N_D = 1 × 10^{22} cm^{-3}, accompanied by J_{SC} = 16.08 mA/cm², V_{OC} = 0.6293 V, and FF = 79.57%. This concentration was retained in subsequent simulations despite practical fabrication constraints that may limit achievable doping levels.

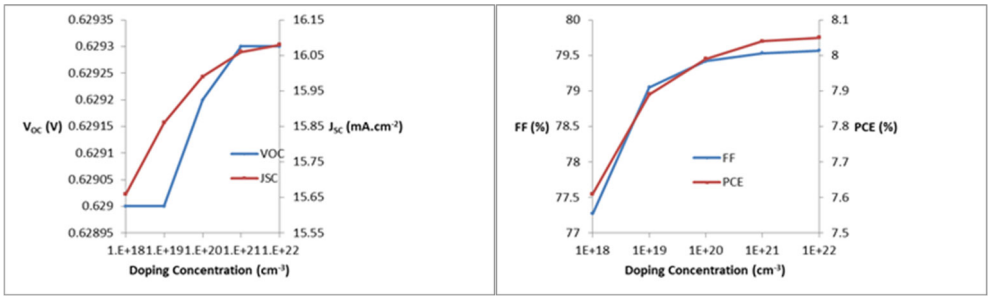

Figure 4. Variation of V_{OC}, J_{SC}, FF, and PCE with donor doping concentration (N_D) in the ETL ($CH_3NH_3SnCl_3$).

3.4. Influence of trap density in the ETL ($CH_3NH_3SnCl_3$)

The density of deep trap states (N_t) within the $CH_3NH_3SnCl_3$ ETL was systematically varied from 10^9 cm^{-3} to 10^{22} cm^{-3} to quantify its impact on the overall

device PCE. The simulation results (**Figure 5**) reveal that V_{OC}, J_{SC}, FF, and PCE remain essentially invariant across the entire N_t sweep, with a consistent maximum PCE of 8.05%. This insensitivity indicates that, under the present device configuration, the ETL trap density is not a performance-limiting factor, likely because carrier transport through the relatively thin 50 nm ETL is dominated by drift rather than diffusion. A value of $N_t = 10^{15}$ cm^{-3} was adopted as the representative ETL trap density for all subsequent stages.

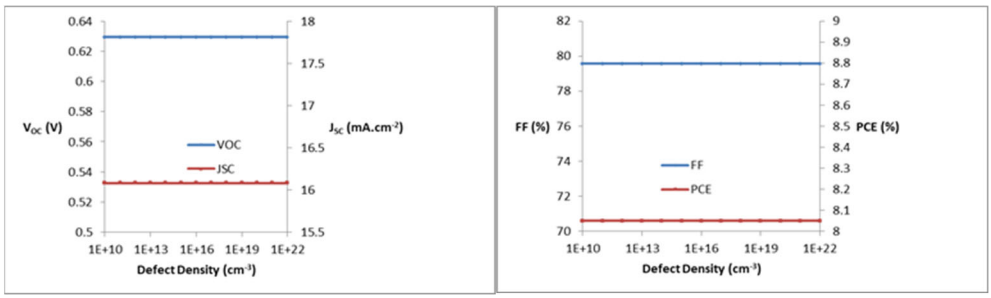

Figure 5. Dependence of V_{OC}, J_{SC}, FF, and PCE on the trap-state density (N_t) in the $CH_3NH_3SnCl_3$ ETL.

4. Effect of the perovskite absorber layer ($CH_3NH_3SnBr_3$) on device performance

Beyond the ETL, the absorber layer fundamentally determines the photovoltaic output of the device by governing the extent of light absorption and the efficiency of exciton dissociation and charge separation. This section systematically evaluates the role of the $CH_3NH_3SnBr_3$ absorber thickness, electron affinity, donor and acceptor doping concentrations, and trap density.

4.1. Absorber layer thickness

The thickness of the light-absorbing layer governs the diffusion length requirement for photogenerated carriers to reach the charge-selective contacts. An unduly thin absorber transmits a fraction of incident photons without absorption, lowering photocurrent and PCE. Conversely, an excessively thick absorber compels carriers to traverse greater distances than their diffusion length permits, resulting in higher series resistance, increased recombination losses, and reduced FF. Identifying the thickness that optimally balances these competing effects is therefore a central design objective.

Absorber thickness was scanned from 25 to 1500 nm while the ETL and HTL parameters remained at their previously optimised values. As recorded in **Figure 6**, J_{SC} increases steadily with absorber thickness as more photons are harvested. V_{OC} also rises with thickness up to a point. However, beyond 200 nm, FF declines because a thicker layer supports a higher density of structural defects that act as non-radiative recombination centres, shortening carrier lifetimes before they can be collected. The PCE reaches its maximum of 19.00% at a thickness of 750 nm, where V_{OC} = 0.7463 V, J_{SC} = 33.60 mA/cm^2, and FF = 75.76%. This 750 nm value was therefore fixed for the remainder of the study.

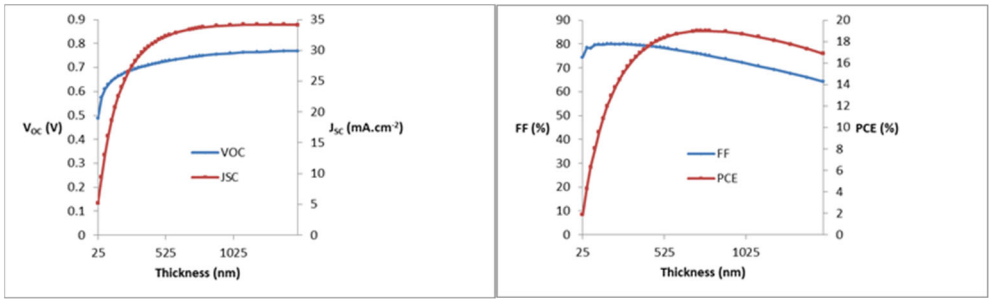

Figure 6. Evolution of V_{OC}, J_{SC}, FF, and PCE as a function of absorber layer thickness for $CH_3NH_3SnBr_3$.

4.2. Electron affinity of the absorber layer

The absorber electron affinity (χ) was varied from 3.40 to 4.17 eV to assess its impact on band alignment and charge-extraction selectivity. As χ was increased, a systematic enhancement in FF was observed. The optimal device performance was obtained at χ = 3.8 eV, as presented in **Figure 7**, where the photovoltaic parameters converged to V_{OC} = 0.8907 V, J_{SC} = 33.69 mA/cm², FF = 78.91%, and PCE = 23.68%. This electron affinity value positions the absorber conduction band in close register with the ETL, minimising electron injection barriers while maintaining a substantial valence band offset that prevents hole leakage into the n-type transport layer.

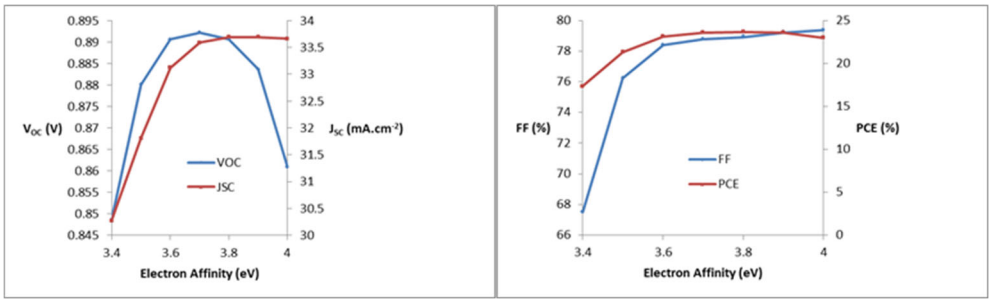

Figure 7. Dependence of V_{OC}, J_{SC}, FF, and PCE on the electron affinity of the $CH_3NH_3SnBr_3$ absorber.

4.3. Donor and acceptor doping in the absorber layer

Controlled doping of the absorber is a well-established strategy to increase carrier density and improve transport properties in perovskite thin films. Both n-type (donor) and p-type (acceptor) configurations are technologically feasible; additionally, unintentional self-doping can arise from non-stoichiometry and lattice imperfections during crystal growth [44-48]. It must be recognised, however, that excessively high doping levels increase defect formation energies and promote Shockley-Read-Hall recombination, which is detrimental to performance [49-51].

For donor doping (N_D), concentrations from 10^{10} cm^{-3} to 10^{19} cm^{-3} were explored while the acceptor concentration and defect density were held constant. **Figure 8a** shows that V_{OC} remains approximately constant up to 10^{13} cm^{-3} before rising to a peak near 10^{17} cm^{-3} and subsequently declining. J_{SC}, FF, and PCE also decrease at N_D beyond 10^{13} cm^{-3}, consistent with increased carrier recombination through impurity states. A maximum efficiency of 23.69% was obtained at $N_D = 10^{10}$

cm^{-3}, alongside J_{SC} = 33.89 mA/cm^2, V_{OC} = 0.8907 V, and FF = 78.94%. This donor concentration was therefore adopted for the n-type absorber channel.

The acceptor doping (N_A) investigation, illustrated in **Figure 8b**, covered the range 10^{10} cm^{-3} to 10^{22} cm^{-3}. A peak efficiency of 24.90% was recorded at $N_A = 10^{16}$ cm^{-3}, with J_{SC} = 33.15 mA/cm^2, V_{OC} = 0.9280 V, and FF = 80.93%. The $CH_3NH_3SnBr_3$ absorber naturally accommodates both donor and acceptor impurities, with carrier type and density governed by the degree of non-stoichiometry in the synthesised crystal [50].

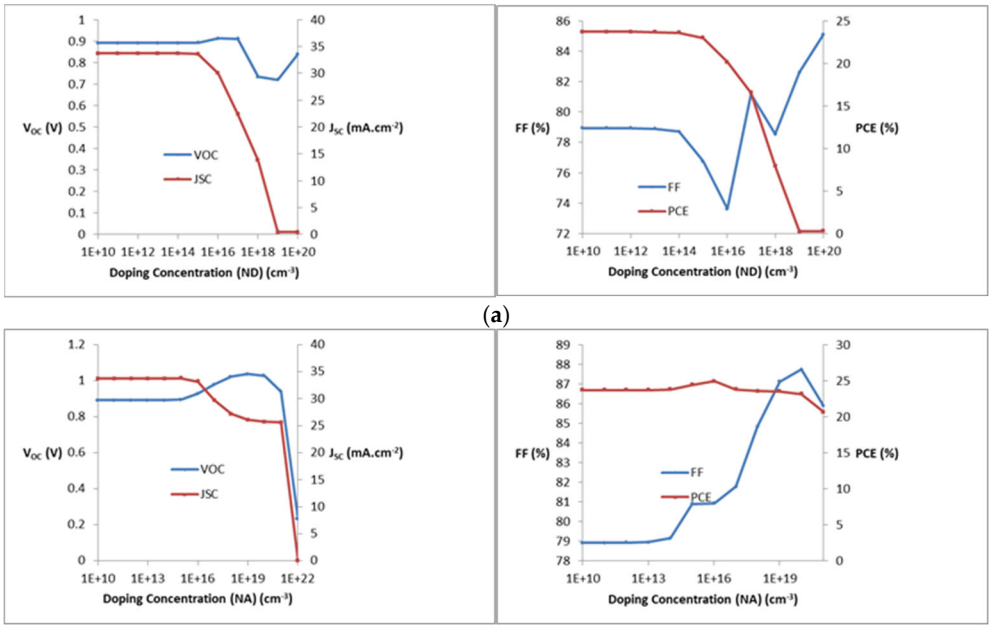

Figure 8. (**a**) Photovoltaic parameters V_{OC}, J_{SC}, FF, and PCE as functions of donor doping concentration (N_D) in the $CH_3NH_3SnBr_3$ absorber. (**b**) Photovoltaic parameters V_{OC}, J_{SC}, FF, and PCE as functions of acceptor doping concentration (N_A) in the $CH_3NH_3SnBr_3$ absorber.

4.4. Trap density in the absorber layer

Despite the progress achieved by tailoring absorber thickness, further gains in efficiency can be realised by controlling the concentration of deep-level trap states within the perovskite bulk. The absorber is the central active region of the device, where the primary photovoltaic processes, photoexcitation, exciton dissociation, carrier transport, and surface recombination, all take place. The microstructural quality of the perovskite film, which is closely tied to its morphology and deposition conditions, governs carrier lifetimes and diffusion lengths and thereby sets the upper bound on extractable photocurrent [52–54].

The absorber trap density N_t was varied over twelve orders of magnitude, from 10^8 cm^{-3} to 10^{20} cm^{-3}, as shown in **Figure 9**. All key figures of merit - J_{SC}, V_{OC}, FF and PCE-decrease progressively as N_t rises, owing to the proliferation of non-radiative recombination pathways that reduce both carrier lifetime and diffusion length. Although the simulation technically permits arbitrarily low defect densities, achieving $N_t \ll 10^{10}$ cm^{-3} in practice would require fabrication conditions that are

prohibitively demanding and that may not be reproducible with currently available deposition methods. Moreover, tin-based perovskites are known to be susceptible to humidity-induced degradation when carrier densities are very low. A pragmatic target of $N_t = 10^{10}$ cm^{-3} was therefore selected, at which the device exhibits PCE = 27.21%, J_{SC} = 33.42 mA/cm², V_{OC} = 0.9579 V, and FF = 84.99%.

This trap-density dependence is well described by the SRH recombination model, in which the recombination rate scales linearly with N_t at low injection levels, confirming that defect engineering is a critical lever for further performance enhancement.

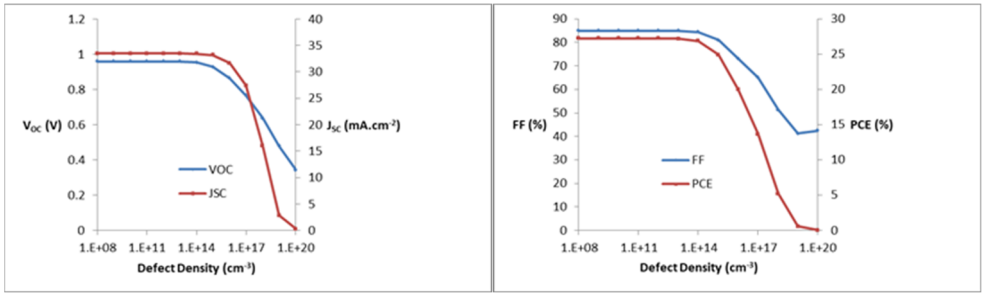

Figure 9. Variation of V_{OC}, J_{SC}, FF, and PCE with absorber trap-state density (N_t) for the $CH_3NH_3SnBr_3$ layer.

5. Effect of the hole transport layer ($CH_3NH_3SnI_3$) on device performance

5.1. HTL thickness

Similar to the ETL investigation, the thickness of the $CH_3NH_3SnI_3$ hole transport layer was swept from 10 to 500 nm, with all previously optimised parameters held fixed. The results, shown in **Figure 10**, confirm that the cell metrics are largely insensitive to HTL thickness across this range-a finding consistent with earlier literature reporting minimal thickness dependence for HTMs that do not need to be optically transparent. An HTL thickness of 200 nm was selected as the practical optimum, yielding an efficiency of 27.21%.

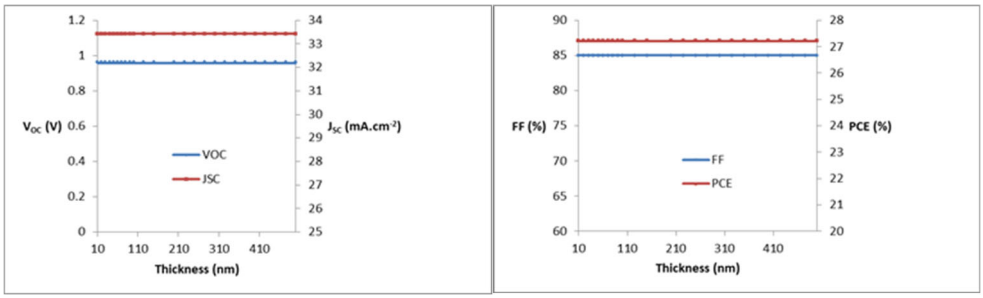

Figure 10. Influence of HTL ($CH_3NH_3SnI_3$) thickness on V_{OC}, J_{SC}, FF, and PCE.

5.2. HTL electron affinity

The electron affinity of the HTL creates a valence band offset at the HTL/absorber interface, which is the primary driving force for selective hole collection. When the electron affinities of adjacent layers are mismatched, a band

offset develops that can either facilitate or impede carrier extraction. In this investigation, χ of $CH_3NH_3SnI_3$ was varied from 3.0 eV to 4.1 eV with its bandgap maintained at 1.3 eV throughout.

As shown in **Figure 11**, V_{OC}, J_{SC}, FF, and PCE all increase monotonically as χ rises from 3.0 to 4.1 eV, above which all parameters stabilise. Within this range, FF climbs from 73.80% to 86.20%, and PCE improves from 9.80% to 28.21%. The efficiency gain at higher affinities is attributable to a reduction in recombination probability at the $CH_3NH_3SnI_3/CH_3NH_3SnBr_3$ heterojunction, which is achieved when the valence band offset between the HTL and absorber is sufficiently large to repel electrons from the p-type contact. Materials with band gaps exceeding 1.3 eV and electron affinities in the 3.5–4.1 eV window are therefore the most suitable HTL candidates for this device architecture. Accordingly, χ = 4.1 eV was fixed as the HTL electron affinity in all subsequent calculations.

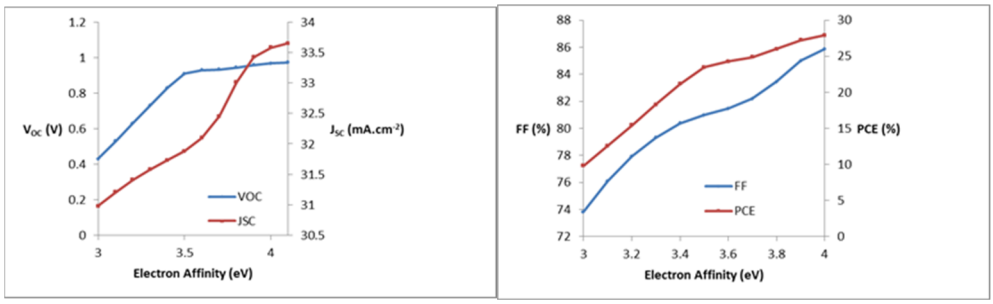

Figure 11. Dependence of V_{OC}, J_{SC}, FF, and PCE on the electron affinity of the $CH_3NH_3SnI_3$ HTL.

5.3. HTL acceptor doping concentration (N_A)

Paralleling the ETL doping study, the acceptor concentration in the $CH_3NH_3SnI_3$ hole transport layer was varied from 10^{10} cm^{-3} to 10^{22} cm^{-3}. As illustrated in **Figure 12**, device efficiency consistently increases with higher HTL doping, because a greater hole density improves the positivity of the HTL and enhances hole-extraction selectivity. Although elevated acceptor concentrations raise the probability of exciton-mediated recombination within the HTL itself, this effect is secondary over the range examined, and efficiency continues to climb toward 10^{22} cm^{-3}. Simultaneously, V_{OC}, J_{SC}, and FF all show trends with increasing Na upward. The optimum HTL acceptor concentration of 10^{22} cm^{-3} was identified, at which the device attains PCE = 31.11%-the best result recorded across the entire parametric study.

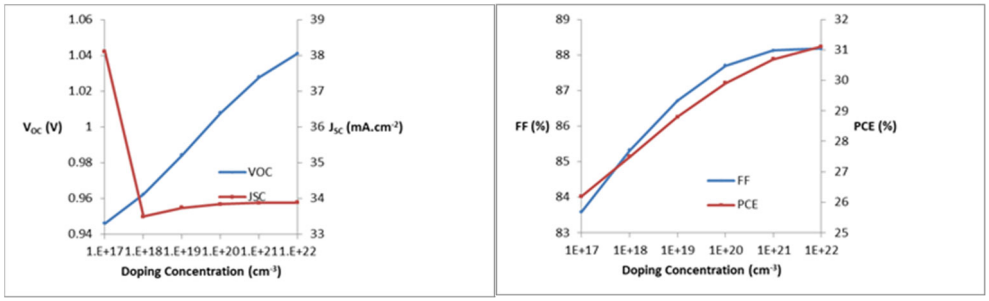

Figure 2. Evolution of V_{OC}, J_{SC}, FF, and PCE with acceptor doping concentration (N_A) in the $CH_3NH_3SnI_3$ HTL.

5.4. HTL trap density

The impact of HTL trap-state density on device performance was examined over the range 10^9–10^{22} cm^{-3} (**Figure 13**). Throughout this sweep, V_{OC}, J_{SC}, and PCE show no appreciable variation, indicating that, under the current device configuration, HTL trap states do not constitute a dominant recombination channel. This insensitivity may stem from the large built-in field at the HTL/absorber interface, which efficiently sweeps holes toward the back contact before trapping events can occur.

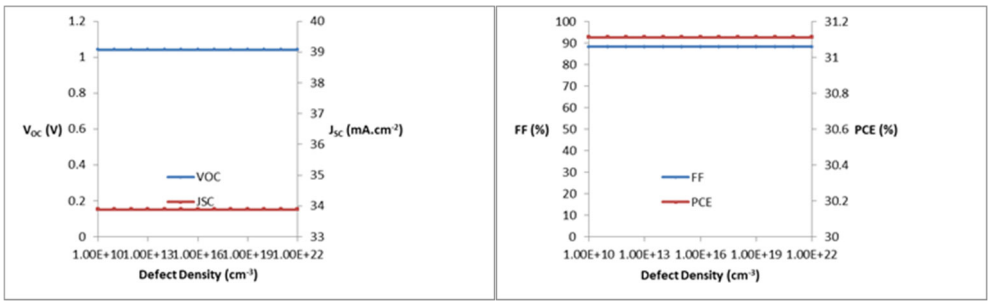

Figure 13. Variation of V_{OC}, J_{SC}, FF, and PCE with trap-state density (N_t) in the $CH_3NH_3SnI_3$ HTL.

6. Thermal stability analysis

Thermal stability constitutes one of the most significant practical challenges for perovskite-based photovoltaics, particularly for applications in hot climates or concentrating systems. Temperature modifies the material bandgap via two distinct lattice-dynamical mechanisms, thermal expansion of the unit cell and thermally activated phonon scattering, both of which narrow the bandgap as temperature rises and thus shift the optical absorption onset. Beyond bandgap modification, elevated temperature accelerates electron-hole recombination rates within the absorber, reduces carrier mobility and perturbs quasi-Fermi level splitting, collectively depressing PCE.

Following the completion of the full parametric optimisation, the temperature-dependent J-V response of the n-i-p device was computed for operating temperatures ranging from 260 K to 450 K (**Figure 14**). The results confirm that temperature exerts a decidedly negative influence on all key photovoltaic metrics. Specifically, as the temperature rose from 300 K to 450 K, V_{OC} fell from 1.0410 V to 0.8425 V,

while J_{SC} remained approximately stable near 34 mA/cm². FF dropped sharply from ~88% to ~81%, and PCE declined from 31.11% to 23.32%. These trends confirm that 300 K is the thermodynamically optimal working point for this device and motivate future experimental efforts to measure degradation kinetics at elevated temperatures for tin-based perovskite cells.

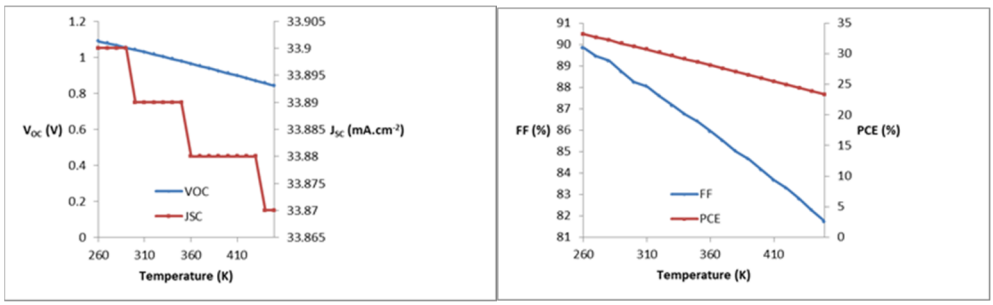

Figure 14. Temperature-dependent photovoltaic outputs-V_{OC}, JSC, FF and PCE-of the optimised n-i-p perovskite solar cell.

7. Series and shunt resistance optimisation

Parasitic resistances within the solar cell circuit represent a practical source of efficiency loss that is distinct from the intrinsic recombination mechanisms discussed above. Series resistance (R_S) aggregates contributions from the ohmic resistance of each functional layer, from contact resistances at metal–semiconductor junctions, and from lateral current spreading in the transparent front electrode. Shunt resistance (R_{SH}), on the other hand, quantifies the magnitude of leakage currents that bypass the p–n junction, typically through pinholes in the absorber film, grain boundary pathways, or partial short circuits at layer interfaces.

In an ideal solar cell, R_S should approach zero and R_{SH} should approach infinity. **Figure 15** illustrates the effect of varying R_S from 0 to 15 Ω·cm². The primary consequence of increasing R_S is a reduction in FF: the fill factor peaks at 88.24% when R_S = 0 Ω·cm² and collapses to 45.53% at 15 Ω·cm², whereas V_{OC} and J_{SC} are only marginally affected. Conversely, as shown in **Figure 16**, increasing R_{SH} strongly enhances PCE by suppressing junction leakage. Experimentally reported values for $CH_3NH_3SnCl_3$-based solar cells fall within R_S = 0–4 Ω·cm² and R_{SH} = 10^4–10^7 Ω·cm², highlighting the importance of minimising interfacial contamination and ensuring pinhole-free absorber deposition.

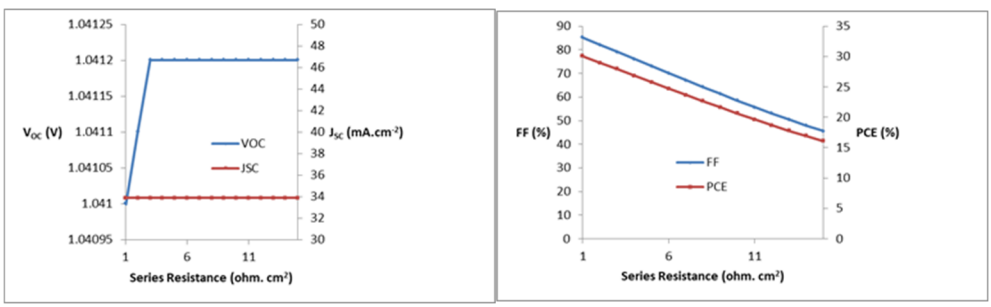

Figure 15. Effect of series resistance (R_S) on the photovoltaic parameters V_{OC}, J_{SC}, FF, and PCE.

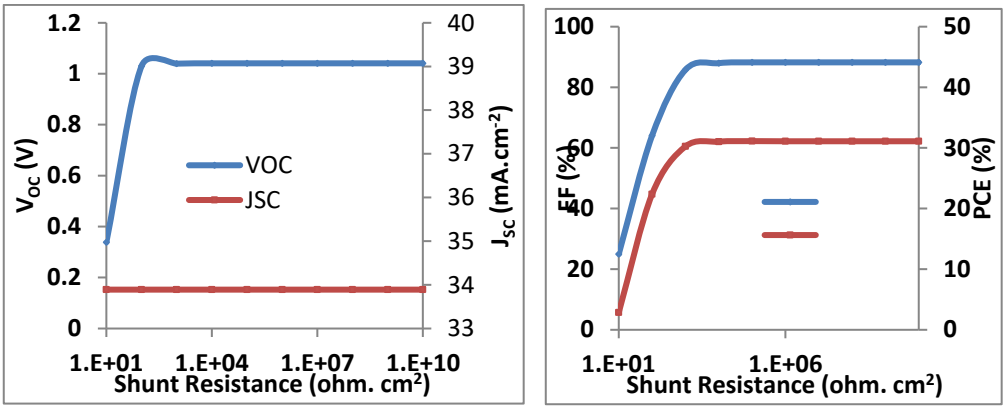

Figure 16. Effect of shunt resistance (R_{SH}) on the photovoltaic parameters V_{OC}, J_{SC}, FF, and PCE.

8. Quantum efficiency analysis

The quantum efficiency (QE) response of the fully optimised cell was simulated across a photon wavelength window of 300–900 nm, as presented in **Figure 17**. In a photovoltaic device, QE at a given wavelength is defined as the ratio of the number of electron-hole pairs collected at the external electrodes to the number of photons incident on the active area at that wavelength. Two spectral regions are identifiable in **Figure 17**. Region I, spanning 300–390 nm, is characterised by a progressively rising QE as the device begins to absorb shorter-wavelength photons. Region II, extending from 390 nm to approximately 860 nm, displays a QE consistently exceeding 90%, a performance attributable to the exceptional minority-carrier diffusion length in high-quality $CH_3NH_3SnBr_3$ crystals and the efficient collection facilitated by the optimised device geometry.

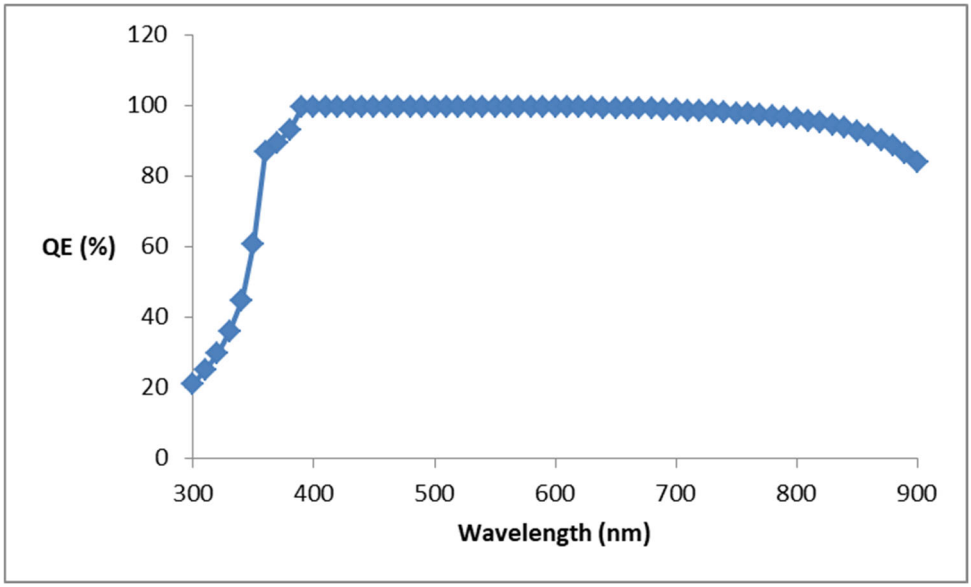

Figure 17 Simulated quantum efficiency (QE) spectrum of the proposed solar cell as a function of incident photon wavelength.

9. Rear electrode work function

The back-contact metal work function determines the magnitude of the ohmic barrier between the HTL valence band and the rear electrode, which governs the built-in potential (V_{bi}) and consequently, the maximum achievable V_{OC}. Practical back-contact options for perovskite cells include gold (Au), silver (Ag), copper (Cu), iron (Fe), and cobalt (Co), whose work functions span the range of approximately 4.6–5.1 eV. When the back-contact work function was varied from 5.1 eV to 5.7 eV (**Figure 18**), V_{OC}, J_{SC}, and FF all remained constant, confirming that the selection of anode material within this work-function window has no significant influence on device performance. This result provides useful flexibility in choosing back-contact metals for fabrication without sacrificing photovoltaic output.

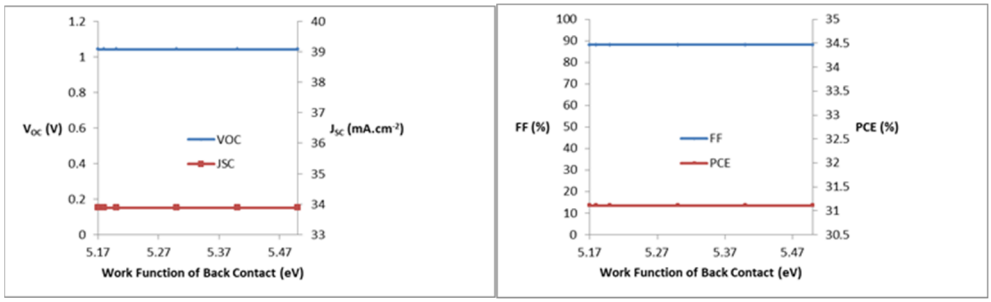

Figure 18. Effect of back-contact work function on the photovoltaic parameters of the proposed solar cell.

10. Optimised device performance: J–V and C–V analysis

The final, fully optimised device configuration is FTO (300 nm)/n-$CH_3NH_3SnCl_3$ (50 nm)/i-$CH_3NH_3SnBr_3$ (750 nm)/p-$CH_3NH_3SnI_3$ (200 nm)/Au, representing a fourfold improvement in PCE over the baseline architecture (7.56% → 31.11%). The complete set of optimised layer parameters is summarised in **Table 3**. **Figure 19** presents the current density–voltage (J–V) characteristic of the optimised cell under AM1.5 G illumination, confirming efficient photocurrent extraction across the full voltage range up to V_{OC}.

Table 3. Optimised design parameters for the proposed lead-free perovskite solar cell.

Physical Parameters	Symbol	Unit	p-$CH_3NH_3SnI_3$ (HTL)	i-$CH_3NH_3SnBr_3$ (Absorber)	n-$CH_3NH_3SnCl_3$ (ETL)
Thickness	t	nm	200	750	50
Electron Affinity	χ	eV	4.1	3.8	3.77
Uniform Shallow Donor Doping	N_D	cm^{-3}	0	1×10^{10}	1×10^{22}
Uniform Shallow Acceptor Doping	N_A	cm^{-3}	1×10^{22}	1×10^{16}	0
Defect Density	N_t	cm^{-3}	1×10^{10}	1×10^{10}	1×10^{15}

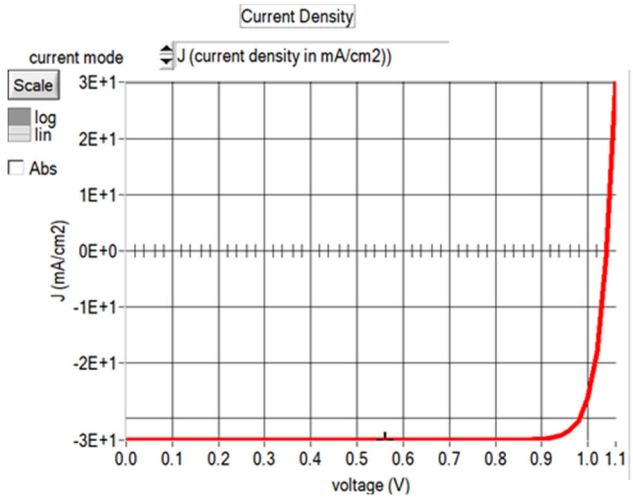

Figure 19. Current density–voltage (J–V) characteristic of the fully optimised FTO/n-$CH_3NH_3SnCl_3$/i-$CH_3NH_3SnBr_3$/p-$CH_3NH_3SnI_3$/Au device.

10.1. Energy band alignment

Correct band alignment between the charge-selective transport layers and the absorber is indispensable for efficient carrier separation in perovskite devices. For the ETL, the conduction band minimum should be energetically close to that of the absorber so that photogenerated electrons face a negligible injection barrier, while the valence band of the ETL should be substantially deeper than that of the absorber to block holes and prevent unwanted hole flow into the n-type layer. For the HTL, the complementary conditions apply: the valence band maximum of the HTL should be well-matched to that of the absorber for efficient hole extraction, while a large conduction band offset prevents electron leakage into the p-type layer. If the conduction band offset between the HTL and absorber is insufficient, electrons can thermally surmount the barrier and recombine at the HTL/Au interface. **Figure 20** depicts the computed energy band diagram of the optimised PSC, confirming that the chosen layer compositions produce a well-graded alignment conducive to carrier separation and collection.

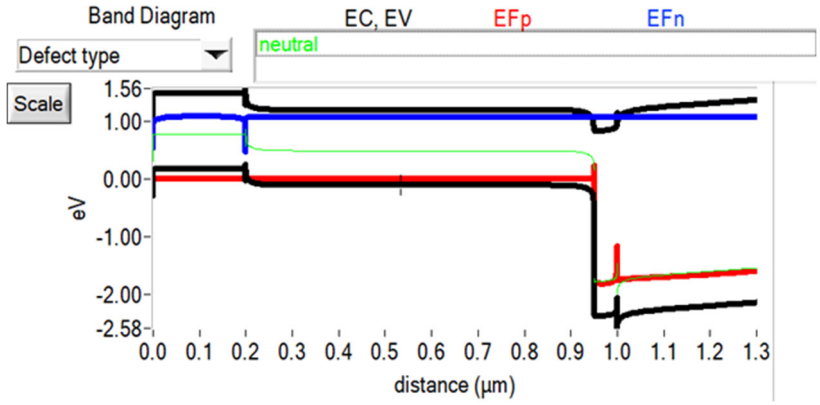

Figure 20. Energy band alignment of the optimised PSC showing conduction and valence band profiles across all layers.

10.2. Capacitance–voltage (C–V) characteristic

The capacitance–voltage (C–V) measurement provides complementary information to the J–V curve, enabling the extraction of the built-in potential (V_{bi}) and the carrier doping density through the Mott–Schottky analysis. The standard Mott–Schottky relations are:

$$\frac{1}{C^2} = \frac{2}{qN_a\varepsilon_0\varepsilon_s A^2}(V_{bi} - V) \tag{6}$$

$$N_a = \frac{2}{q\varepsilon_0\varepsilon_s A^2 [\frac{d}{d_v}\frac{1}{C^2}\}} \tag{7}$$

where $\varepsilon_0 = 8.85 \times 10^{-14}$ F cm^{-1} is the permittivity of free space, N_a is the acceptor doping density (cm^{-3}), $q = 1.6 \times 10^{-19}$ C is the elementary charge, ε_s is the relative dielectric constant of the semiconductor, A is the device area (cm^2), C is the measured capacitance, and V is the applied bias. **Figure 21** displays the $1/C^2$ versus V (Mott–Schottky) plot, from which V_{bi} was determined to be 1.3 V for the $CH_3NH_3SnCl_3$-based heterostructure. The relatively large built-in potential corroborates the high PCE recorded in this study by confirming that a substantial electrostatic driving force is available to separate photogenerated carriers and deliver them to the respective contacts.

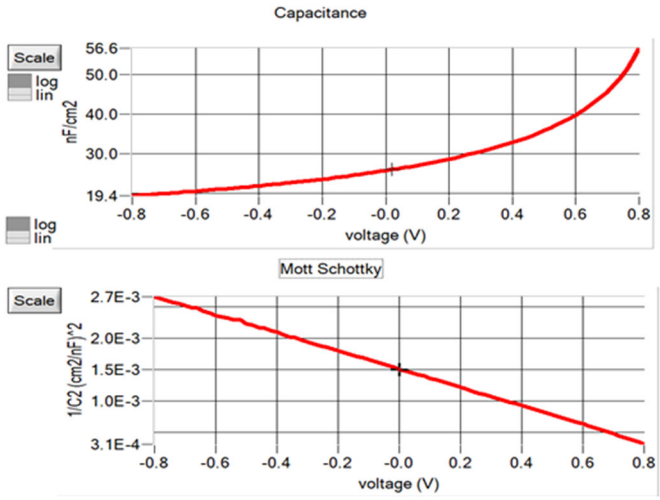

Figure 21. Mott–Schottky ($1/C^2$ vs V) plot for the optimised perovskite heterostructure solar cell.

11. Conclusions

A lead-free n-i-p perovskite solar cell based on the tin halide heterostructure FTO (300 nm)/n-$CH_3NH_3SnCl_3$ (50 nm)/i-$CH_3NH_3SnBr_3$ (750 nm)/p-$CH_3NH_3SnI_3$ (200 nm)/Au was numerically designed and comprehensively optimised using the SCAPS-1D device simulator. A sequential parametric investigation of layer thickness, electron affinity, shallow doping, and trap density across all functional layers produced a systematic improvement in photovoltaic performance. The key optimised design values were: ETL thickness of 50 nm with $\chi = 3.77$ eV; absorber thickness of 750 nm with $\chi = 3.8$ eV; and HTL thickness of 200 nm with $\chi = 4.1$ eV. Doping concentrations were fixed at $N_D = 1 \times 10^{22}$ cm^{-3} for the ETL, $N_D = 1 \times 10^{10}$ cm^{-3} and $N_A = 1 \times 10^{16}$ cm^{-3} for the absorber, and $N_A = 1 \times 10^{22}$ cm^{-3} for the HTL.

The optimised device delivered a PCE of 31.11%, J_{SC} = 33.89 mA/cm², V_{OC} = 1.0410 V, and FF = 88.18%-a fourfold improvement over the unoptimised baseline. Thermal analysis confirmed that 300 K represents the ideal operating temperature, beyond which carrier recombination and bandgap narrowing progressively erode performance. These results collectively affirm the potential of all-tin halide perovskite architectures as environmentally sustainable, high-efficiency alternatives to incumbent lead-based photovoltaic technologies. Experimental validation and tandem cell integration are identified as logical next steps to translate these simulation predictions into practical devices.

Acknowledgements: We would like to express our gratitude to Dr. Marc Burgelman and their team from Ghent University, Belgium, for providing access to the SCAPS simulator, which has been instrumental in conducting the simulations for this research. This work is supported by the research project (Project ID 3847) funded by the Council of Science and Technology, Uttar Pradesh, India as per letter no. CST/D-826.

References

1. Yang Z; Guo Y; Li H; Zhou Y; Zuo X; Yu Y; Pan C; Strzalka J; Nam CY; Rafailovich MH. Roles of Interfacial Tension in Regulating Internal Organization of Low Bandgap Polymer Bulk Heterojunction Solar Cells by Polymer Additives. Advanced Materials Interfaces. 2018, 5, 1800435.
2. Noel NK; Stranks SD; Abate A; Wehrenfennig C; Guarnera S; Haghighirad AA; Sadhanala A; Eperon GE; Pathak SK; Johnston MB; et al. Lead-Free Organic–Inorganic Tin Halide Perovskites for Photovoltaic Applications. Energy & Environmental Science. 2014, 7, 3061–3068.
3. Kim JY; Lee JW; Jung HS; Shin H; Park NG. High-Efficiency Perovskite Solar Cells. Chemical Reviews. 2020, 120, 7867–7918.
4. Liang FC; Jhuang FC; Fang YH; Benas JS; Chen WC; Yan ZL; Lin WC; Su CJ; Sato Y; Chiba T; et al. Synergistic Effect of Cation Composition Engineering of Hybrid $Cs_{1-x}FA_xPbBr_3$ Nanocrystals for Self-Healing Electronics Application. Advanced Materials. 2023, 35, 2207617.
5. Ma C; Park NG. A Realistic Methodology for 30% Efficient Perovskite Solar Cells. Chem. 2020, 6, 1254–1264.
6. Abate A. Perovskite Solar Cells Go Lead Free. Joule. 2017, 1, 659–664.
7. Mahajan P; Datt R; Chung Tsoi W; Gupta V; Tomar A; Arya S. Recent Progress, Fabrication Challenges and Stability Issues of Lead-Free Tin-Based Perovskite Thin Films in the Field of Photovoltaics. Coordination Chemistry Reviews. 2021, 429, 213633.
8. Sabbah H; Arayro J; Mezher R. Numerical Simulation and Optimization of Highly Stable and Efficient Lead-Free Perovskite $FA_{1-x}Cs_xSnI_3$-Based Solar Cells Using SCAPS. Materials. 2022, 15, 4761.
9. Xu K. Development of Tin-Based Perovskite Materials for Solar Cell Applications: A Minireview. Instrumentation Science & Technology. 2021, 49, 91–105.
10. Cao J; Yan F. Recent Progress in Tin-Based Perovskite Solar Cells. Energy & Environmental Science. 2021, 14, 1286–1325.
11. Ke W; Kanatzidis MG. Prospects for Low-Toxicity Lead-Free Perovskite Solar Cells. Nature Communications. 2019, 10, 965.
12. Stoumpos CC; Malliakas CD; Kanatzidis MG. Semiconducting Tin and Lead Iodide Perovskites with Organic Cations: Phase Transitions, High Mobilities, and Near-Infrared Photoluminescent Properties. Inorganic Chemistry. 2013, 52, 9019–9038.
13. Marshall KP; Walker M; Walton RI; Hatton RA. Enhanced Stability and Efficiency in Hole-Transport-Layer-Free $CsSnI_3$ Perovskite Photovoltaics. Nature Energy. 2016, 1, 16178.
14. Herz LM. Charge-Carrier Mobilities in Metal Halide Perovskites: Fundamental Mechanisms and Limits. ACS Energy Letters. 2017, 2, 1539–1548.

15. Rajendra Kumar G; Kim HJ; Karupannan S; Prabakar K. Interplay between Iodide and Tin Vacancies in $CsSnI_3$ Perovskite Solar Cells. Journal of Physical Chemistry C. 2017, 121, 16447–16453.
16. Liao Y; Liu H; Zhou W; Yang D; Shang Y; Shi Z; Li B; Jiang X; Zhang L; Quan LN; et al. Highly Oriented Low-Dimensional Tin Halide Perovskites with Enhanced Stability and Photovoltaic Performance. Journal of the American Chemical Society. 2017, 139, 6693–6699.
17. Shukla RK, Srivastava A, Rani S, Singh N, Dwivedi VK, Pandey S, & Wadhwani N. (2024). Modeling for Efficiency Enhancement of Perovskite Thin-Film Solar Cell by Using Double-Absorber and Buffer Layers. Integrated Ferroelectrics. 240(1), 73–91.
18. Shukla RK, Srivastava A, Rani S, et al.: Simulation study of solar cell with a double absorber layers of perovskites material using lead and lead-free material. Journal of Optics. (2024).
19. Shukla RK, Srivastava A, Rani S, Singh N, Dwivedi VK, Pandey S, Wadhwani N.: Simulation and evaluation of perovskite solar cells utilizing various electron transport layers. Nanosystems: Physics, Chemistry, Mathematics. 2024, 15 (1), 135–146.
20. Mishra A, Shukla RK: Simulation of photovoltaic material (donor blends PTB7:PC70BM) polymer for solar cell application. Materials Today: Proceedings. 2021, 46, 2288–2293.
21. Mishra A, Shukla RK: Effect of humidity in the perovskite solar cell. Materials Today: Proceedings. 2020, 29, 836–838.
22. Mei A; Li X; Liu L; Ku Z; Liu T; Rong Y; et al. A Hole-Conductor–Free, Fully Printable Mesoscopic Perovskite Solar Cell with High Stability. Science. 2014, 345, 295–298.
23. Arya S; Mahajan P; Gupta R; Srivastava R; Tailor NK; et al. A Comprehensive Review on Synthesis and Applications of Single Crystal Perovskite Halides. Progress in Solid State Chemistry. 2020, 60, 100286.
24. Grätzel M. The Light and Shade of Perovskite Solar Cells. Nature Materials. 2014, 13, 838–842.
25. Boix PP; Agarwala S; Koh TM; Mathews N; Mhaisalkar SG. Perovskite Solar Cells: Beyond Methylammonium Lead Iodide. Journal of Physical Chemistry Letters. 2015, 6, 898–907.
26. Jacak JE; Jacak WA. Routes for Metallization of Perovskite Solar Cells. Materials. 2022, 15, 2254.
27. Wu R; Yang B; Zhang C; Huang Y; Cui Y; Liu P; et al. Prominent Efficiency Enhancement in Perovskite Solar Cells Employing Silica-Coated Gold Nanorods. Journal of Physical Chemistry C. 2016, 120, 6996–7004.
28. Laska M; Krzeminska Z; Kluczyk-Korch K; Schaadt D; Popko E; Jacak WA; Jacak JE. Metallization of Solar Cells, Exciton Channel of Plasmon Photovoltaic Effect in Perovskite Cells. Nano Energy. 2020, 75, 104751.
29. Yao K; Zhong H; Liu Z; Xiong M; Leng S; Zhang J; et al. Plasmonic Metal Nanoparticles with Core–Bishell Structure for High-Performance Organic and Perovskite Solar Cells. ACS Nano. 2019, 13, 5397–5409.
30. Shao S; Liu J; Portale G; Fang HH; Blake GR; et al. Highly Reproducible Sn-Based Hybrid Perovskite Solar Cells with 9% Efficiency. Advanced Energy Materials. 2018, 8, 1702019.
31. Lee SJ; Shin SS; Kim YC; Kim D; Ahn TK; Noh JH; Seo J; Seok SI. Fabrication of Efficient Formamidinium Tin Iodide Perovskite Solar Cells through SnF_2–Pyrazine Complex. Journal of the American Chemical Society. 2016, 138, 3974–3977.
32. Chen K; Wu P; Yang W; Su R; Luo D; Yang X; et al. Low-Dimensional Perovskite Interlayer for Highly Efficient Lead-Free Formamidinium Tin Iodide Perovskite Solar Cells. Nano Energy. 2018, 49, 411–418.
33. Ke W; Stoumpos CC; Zhu M; Mao L; Spanopoulos I; Liu J; et al. Enhanced Photovoltaic Performance and Stability with a New Type of Hollow 3D Perovskite $FASnI_3$. Science Advances. 2017, 3, e1701293.
34. Wang F; Ma J; Xie F; Li L; Chen J; Fan J; Zhao N. Organic Cation-Dependent Degradation Mechanism of Organotin Halide Perovskites. Advanced Functional Materials. 2016, 26, 3417–3423.
35. Baig F; Khattak YH; Mari B; Beg S; Ahmed A; Khan K. Efficiency Enhancement of $CH_3NH_3SnI_3$ Solar Cells by Device Modeling. Journal of Electronic Materials. 2018, 47, 5275–5282.
36. Du HJ; Wang WC; Zhu JZ. Device Simulation of Lead-Free $CH_3NH_3SnI_3$ Perovskite Solar Cells with High Efficiency. Chinese Physics B. 2016, 25, 108802.
37. Burgelman M; Nollet P; Degrave S. Modelling Polycrystalline Semiconductor Solar Cells. Thin Solid Films. 2000, 361–362, 527–532.
38. Dang Y; Zhou Y; Liu X; Ju D; Xia S; Xia H; Tao X. Formation of Hybrid Perovskite Tin Iodide Single Crystals by Top-Seeded Solution Growth. Angewandte Chemie International Edition. 2016, 55, 3447–3450.
39. Gamal N; Sedky SH; Shaker A; Fedawy M. Design of Lead-Free Perovskite Solar Cell Using $Zn_{1-x}Mg_xO$ as ETL: SCAPS Device Simulation. Optik. 2021, 242, 167306.

40. Valeti NJ, Prakash K, Singha MK. Numerical simulation and optimization of lead free $CH_3NH_3SnI_3$ perovskite solar cell with $CuSbS_2$ as HTL using SCAPS 1D. Results in Optics. 2023, 12, 100440.
41. Rawat S, Madan J and Pandey R. Investigation of $CH_3NH_3SnBr_3$ Perovskite as an Active Layer in PV Cells: SCAPS-1D Simulation and Thickness Optimization for Enhanced Efficiency. ICSSES, Tumakuru, India, 2023, pp. 1–4.
42. Yasin S; Al-Zoubi T; Moustafa M. Design and Simulation of High Efficiency Lead-Free Heterostructure Perovskite Solar Cell Using SCAPS-1D. Optik. 2021, 229, 166258.
43. Rahman MS; Miah S; Marma MSW; Sabrina T. Simulation Based Investigation of Inverted Planar Perovskite Solar Cell with All Metal Oxide Inorganic Transport Layers. In Proc. ECCE, Cox's Bazar, Bangladesh, 2019; pp. 1–6.
44. Park BW, et al. Bismuth based hybrid perovskites $A_3Bi_2I_9$ (A: methylammonium or cesium) for solar cell application. Advanced Materials. 2015, 27(43), 6806–6813.
45. Miyasaka T, et al. Perovskite solar cells: can we go organic-free, lead-free, and dopant-free. Advanced Energy Materials. 2020, 10(13), 1902500.
46. Zhou Y, Zhao Y. Chemical stability and instability of inorganic halide perovskites. Energy & Environmental Science. 2019, 12(5), 1495–1511.
47. Zyoud SH, Zyoud AH, Ahmed NM, et al. Numerical Modeling of High Conversion Efficiency FTO/ZnO/CdS/CZTS/MO Thin Film-Based Solar Cells Using SCAPS-1D. Crystals. 2021, 11(12), 1468.
48. Chen H, et al. Inorganic perovskite solar cells: a rapidly growing field. Solar RRL. 2018, 2(2), 1700188.
49. Brandt RE, et al. Identifying defect-tolerant semiconductors with high minority-carrier lifetimes: beyond hybrid lead halide perovskites. MRS Communications. 2015, 5(2), 265–275.
50. Patel M, Ray A. Enhancement of output performance of Cu_2ZnSnS_4 thin film solar cells – A numerical simulation approach and comparison to experiments. Physica B: Condensed Matter. 2012, 407, 4391–4397.
51. Zhang J, Shao L. Cu_2ZnSnS_4 thin films prepared by sulfurizing different multilayer metal precursors. Science China Technological Sciences. 2009, 52, 269–272.
52. Kim H; Lim KG; Lee TW. Planar heterojunction organometal halide perovskite solar cells: roles of interfacial layers. Energy & Environmental Science. 2016, 9, 12–30.
53. Ball JM; Lee MM; Hey A; Snaith HJ. Low temperature processed meso-superstructure to thin-film perovskite solar cells. Energy & Environmental Science. 2013, 6, 1739–1743.
54. Barbe J; Tietze ML; Neophytou M; Murali B; Alarousu E; El Labban A; Abulikemu M; Yue W; Mohammed OF; McCulloch I; Amassian A; Del Gobbo S. Amorphous tin oxide as a low-temperature-processed electrontransport layer for organic and hybrid perovskite solar cells. ACS Applied Materials & Interfaces. 2017, 9, 11828–11836.